Inorganic Chemistry

Article

pubs.acs.org/IC

Synthesis, Structural Characterization, and Physical Properties of the New Transition Metal Oxyselenide $Ce_2O_2ZnSe_2$

Chris M. Ainsworth,[†] Chun-Hai Wang,[†] Matthew G. Tucker,[‡] and John S. O. Evans*[,†]

[†]Department of Chemistry, University Science Site, Durham University, South Road, Durham DH1 3LE, United Kingdom

[‡]ISIS Neutron and Muon Source, Science and Technology Facilities Council, Rutherford Appleton Laboratory, Harwell Oxford, Didcot OX11 0QX, United Kingdom

Supporting Information

ABSTRACT: The quaternary transition metal oxyselenide $Ce_2O_2ZnSe_2$ has been shown to adopt a ZrCuSiAs-related structure with Zn^{2+} cations in a new ordered arrangement within $[ZnSe_2]^{2-}$ layers. The color of the compound changes as a function of cell volume, which can vary by ∼0.4% under different synthetic conditions. At the highest, intermediate, and lowest cell volumes, the color is yellow-ochre, brown, and black, respectively. The decreased volume is attributed to oxidation of Ce from 3+ to 4+, the extent of which can be controlled by synthetic conditions. $Ce_2O_2ZnSe_2$ is a semiconductor at all cell volumes with experimental optical band gaps of 2.2, 1.4, and 1.3 eV for high, intermediate, and low cell volume samples, respectively. SQUID measurements show $Ce_2O_2ZnSe_2$ to be paramagnetic from 2 to 300 K with a negative Weiss temperature of $\theta = -10$ K, suggesting weak antiferromagnetic interactions.

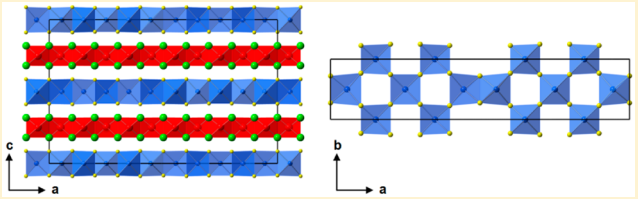

INTRODUCTION

Since the 2008 discovery of superconductivity at ∼26 K in F-doped LaOFeAs,[1] mixed anion materials have been studied extensively. Recently, superconductivity has been reported in structurally related oxychalcogenides such as $Bi_4O_4S_3$ (T_c up to 8.6 K),[2−4] $LnO_{1-x}F_xBiS_2$ (Ln = La, Ce, Pr, Nd, Yb; T_c 1.9−4.5 K),[5] and $LaO_{0.5}F_{0.5}BiSe_2$ (T_c 2.6 K).[6] Issues with sample purity have led to some controversy over the superconducting phase in these systems, with $Bi_3O_2S_3$ suggested to be the superconducting phase in the $Bi_4O_4S_3$ system.[7,8] Superconductivity aside, many oxychalcogenides have other interesting electronic, magnetic, and optical properties. For example, LaCuOS is a wide band gap p-type semiconductor with an optical band gap of 3.1 eV that can be acceptor-doped to give room-temperature conductivity up to 2.6×10^{-1} S cm^{-1}.[9]

LaCuOS and analogous LnOCuCh (Ln = La−Nd, Bi; Ch = S, Se, Te) materials adopt the tetragonal ZrCuSiAs structure with space group *P*4/*nmm*. The structure is built up from alternating layers of fluorite-like $[Ln_2O_2]^{2+}$ and anti-fluorite-like $[Cu_2Ch_2]^{2-}$ sheets.[10,11] There has been recent interest in compounds related to LnOCuCh with divalent transition metal ions. This divalency leads to half occupancy of the transition metal sites giving $[MSe_2]^{2-}$ layers, the ordering of which can be complex. The first of these materials, $Ce_2O_2MnSe_2$, was reported as having random 50% statistical occupancy of Mn on each site.[12] This arrangement retains the tetragonal space group *P*4/*nmm* of LnOCuCh-type compounds. Other work in our group shows that this random distribution is incorrect; however, the *P*4/*nmm* structure provides a useful parent or "subcell" model in which to initially identify ZrCuSiAs-related compounds and from which to consider the structural relationships between materials. $Ce_2O_2FeSe_2$ has $[FeSe_2]^{2-}$ layers containing one-dimensional chains of exclusively edge-sharing (E, stripe-like) $FeSe_4$ tetrahedra,[13] whereas $La_2O_2CdSe_2$ has $[CdSe_2]^{2-}$ layers containing exclusively corner-sharing (C, checkerboard-like) $CdSe_4$ tetrahedra.[14] $La_2O_2ZnSe_2$ has $[ZnSe_2]^{2-}$ layers containing sections of both stripe-like edge-sharing $ZnSe_4$ tetrahedra and checkerboard-like corner-sharing $ZnSe_4$ tetrahedra.[15] It can therefore be considered as an intermediate structure between $Ce_2O_2FeSe_2$ and $La_2O_2CdSe_2$. These different ordering patterns are illustrated in Figure 1.

We report here the synthesis and characterization of the new transition metal oxyselenide $Ce_2O_2ZnSe_2$, which displays different structural and physical properties depending on the synthetic conditions. Structural characterization indicates that Zn^{2+} cations display a novel ordering pattern within the $[ZnSe_2]^{2-}$ layers. The structure was determined by first establishing the unit cell volume by electron diffraction and Pawley fitting of X-ray powder diffraction (XRPD) data, followed by symmetry-adapted distortion mode analysis to determine the Zn^{2+} ordering pattern. This is complemented by neutron powder diffraction data. Diffuse reflectance measurements show that $Ce_2O_2ZnSe_2$ is a semiconductor, though the bandgap is dependent on the synthetic conditions. SQUID measurements show that $Ce_2O_2ZnSe_2$ is paramagnetic from 2 to 300 K.

Received: October 24, 2014
Published: January 13, 2015

DOI: 10.1021/ic502551n
Inorg. Chem. 2015, 54, 1563−1571

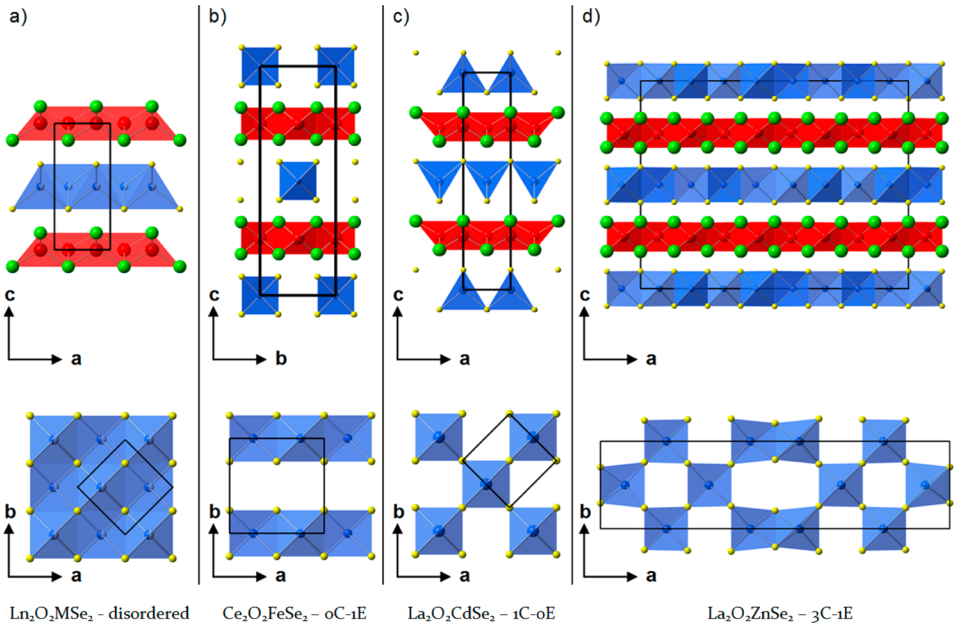

Figure 1. ZrCuSiAs-derived structures reported for (a) $Ln_2O_2MSe_2$, *P4/nmm* symmetry, (b) $Ce_2O_2FeSe_2$, *Imcb* symmetry, (c) $La_2O_2CdSe_2$, $P4_2/nmc$ symmetry, and (d) $La_2O_2ZnSe_2$, *Bmab* symmetry. The top figures show the fluorite-like sheets of edge-sharing Ln_4O tetrahedra (red) and anti-fluorite-like sheets of MSe_4 tetrahedra (blue). Bottom figures are the view down [001], showing the arrangement of MSe_4 tetrahedra. Ln^{3+} cations are shown in green, O^{2-} anions in red, M^{2+} cations in blue, and Se^{2-} anions in yellow.

EXPERIMENTAL SECTION

Polycrystalline samples of $Ce_2O_2ZnSe_2$ were prepared by reaction of CeO_2 (99.99%, Alfa Aesar, heated to 1000 °C before use), Zn (99.9%, Sigma Adrich), and Se (99.999%, Alfa Aesar) powders in a 1:2:1 ratio. Reagents were intimately ground and placed in an alumina crucible. Al powder (99.5% Alfa Aesar) was placed in a second alumina crucible to act as an oxygen getter (forming Al_2O_3 during the reaction). These two crucibles were placed in an evacuated ($<10^{-3}$ atm) silica tube and slowly heated to a final dwell temperature for a set time before cooling to room temperature. The equation for the reaction is

$$2CeO_2 + Zn + 2Se + \frac{4}{3}Al \rightarrow Ce_2O_2ZnSe_2 + \frac{2}{3}Al_2O_3$$

The effect of final dwell temperature was investigated at 1100, 1150, 1175, 1200, and 1225 °C, with the final dwell time fixed at 12 h and the aluminum oxygen getter (AOG) molar amount fixed at 110% (i.e., 10% molar excess). The effect of final dwell time was investigated by holding at 1200 °C for 1, 3, 6, 9, 12, and 24 h with 110% AOG. The effect of AOG quantity was investigated by using molar amounts of 90, 95, 100, 105, and 110% at 1200 °C for 12 h. In each case, 0.6 g of sample was prepared.

For neutron powder diffraction (NPD) experiments at ISIS, a large sample (~2.4 g) was made by synthesizing four 0.6 g samples at 1200 °C with a 12 h dwell time and 110% AOG. These four samples were then intimately ground together and reheated for 12 h at 1200 °C in an evacuated silica tube containing 0.002 g of Se. This synthesis method was preferred for the neutron sample because it contained only a single impurity phase (~5% Ce_2O_2Se) and gave a low cell volume sample with superstructure peaks that could be indexed on a commensurate unit cell. ***Experimental warning:*** *attempts to synthesize more than 0.6 g at 1200 °C (where silica starts to soften) in a single tube can lead to the tube swelling and ultimately bursting.*

X-ray powder diffraction (XRPD) data were collected using a Bruker D8 diffractometer operating in reflection mode with Cu $K\alpha_{1/2}$ radiation, Lynxeye Si strip PSD, a 0.02° step size, and variable slits. Samples were sprinkled onto Si zero-background slides covered with a thin layer of Vaseline. For initial phase identification and cell parameter determination, room-temperature data were collected for 30 min over a 2θ range of 8–120°. Where more detailed structural information and/or XRPD patterns are presented, room-temperature data were collected for 14 h over a 2θ range of 8–120° unless specified otherwise. NPD data for Rietveld analysis were collected on the GEM diffractometer at ISIS. Approximately 2.4 g of sample was loaded into a 6 mm diameter cylindrical vanadium can, and data were acquired for 2 h at room temperature. Powder diffraction data were analyzed by the Rietveld method[16] using Topas Academic (TA) software.[17−19] A combined X-ray and neutron (6 detector banks) refinement was carried out using room-temperature scans. The background (shifted Chebychev), sample height (DIFA/DIFC/ZERO for neutron refinements), peak profiles, March Dollase unidirectional preferred orientation correction[20] along 001 (X-ray only), Pitschke surface roughness correction,[21] lattice parameters, atomic positions, isotropic thermal parameters, absorption correction, and phase fraction of the Ce_2O_2Se impurity phase (~5 wt %) were refined.

Selected area electron diffraction (SAED) data were collected using a Jeol 2100F transmission electron microscope operating at 200 keV. The sample was deposited onto a holey carbon grid, which was mounted in a double-tilt sample holder, and zone axis diffraction patterns were acquired using a Gatan Orius CCD camera.

Diffuse reflectance spectra were obtained by illumination of samples using an Energetiq LDLS EQ-99 broadband lamp and collected at 20° to the excitation using Ocean Optics software; integration times were adjusted to afford maximum response of the spectrometer without saturating the detector. NaCl was used as a reference. Data were used to calculate the reflectance spectra $R(I)$ and then analyzed using Kubelka–Munk treatment.[22,23]

Magnetic measurements were carried out using a Quantum Design SQUID magnetometer in the temperature range of 2–300 K on samples (~0.1 g) mounted in gelatin capsules. During the measurement, a 1000 Oe field was applied.

RESULTS AND DISCUSSION

Synthesis and Phase Purity. Samples of $Ce_2O_2ZnSe_2$ were initially synthesized for 12 h with an AOG molar amount of 110% at 1100, 1150, 1175, 1200, and 1225 °C. XRPD data showed that a ZrCuSiAs-related phase had formed in varying amounts with a unit cell of $a \approx 4.01$ Å and $c \approx 8.86$ Å (the subcell), explaining the main peaks in the XRPD pattern. Weak additional reflections were observed at low angles (Figure S1 of

DOI: 10.1021/ic502551n
Inorg. Chem. 2015, 54, 1563–1571

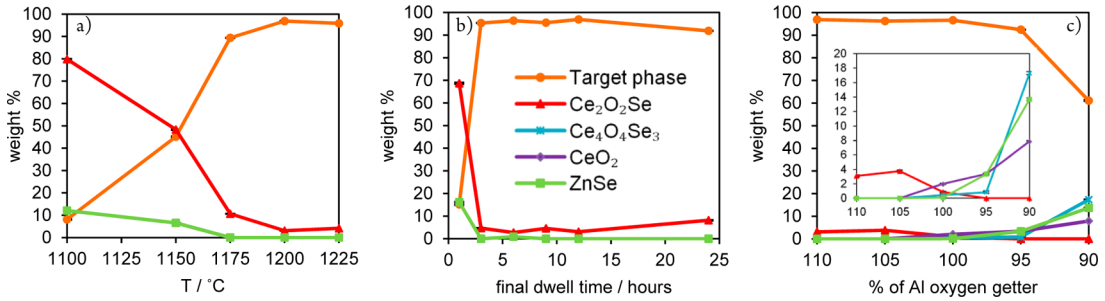

Figure 2. (a) Effect of temperature on the weight % of $Ce_2O_2ZnSe_2$ formed, with the time and AOG molar amount fixed at 12 h and 110%, respectively. (b) Effect of dwell time on the $Ce_2O_2ZnSe_2$ weight fraction (1200 °C and 110% AOG). (c) Effect of AOG molar ratio on $Ce_2O_2ZnSe_2$ weight % (1200 °C, 12 h); inset: *y* scale from 0 to 20% to show impurity phase weight fractions more clearly. Rietveld error bars are hidden by data points. More realistic error bars are around ±2%.

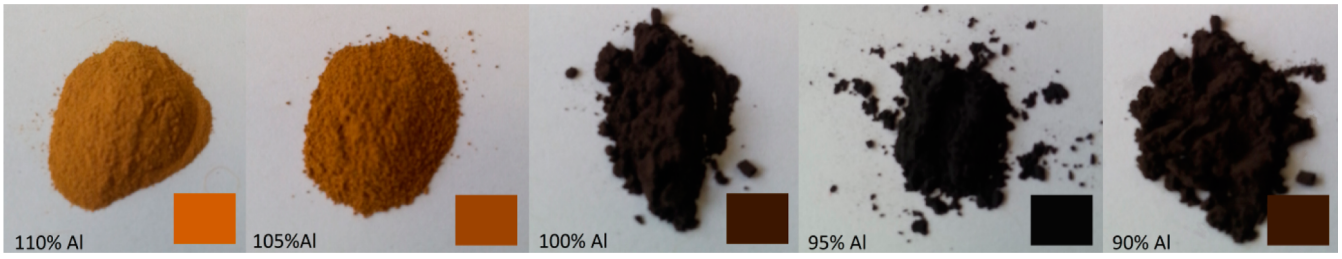

Figure 3. Powder samples synthesized with a range of AOG ratios at 1200 °C for 12 h. Samples are yellow-ochre, brown, and black at relative high, intermediate, and low cell volumes, respectively.

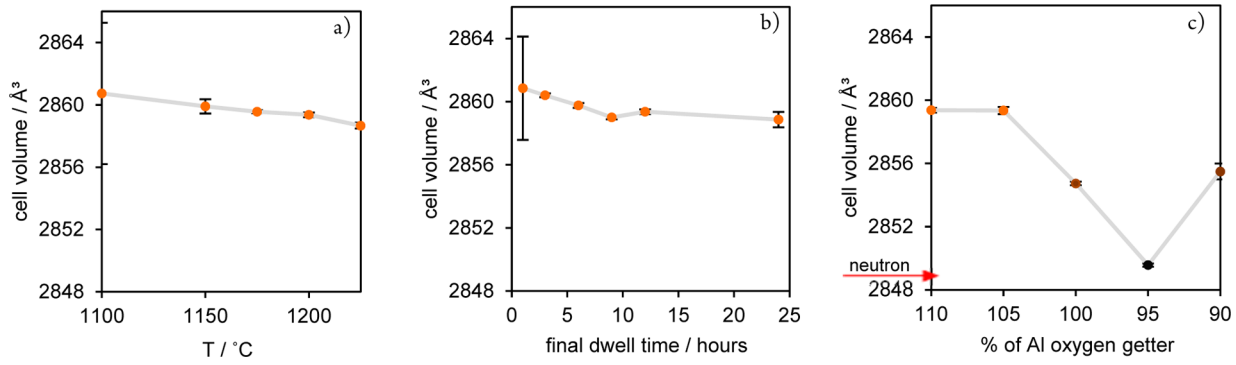

Figure 4. (a) Effect of synthesis temperature on cell volume (12 h and 110% AOG). (b) Effect of dwell time on cell volume (1200 °C and 110% AOG). (c) Effect of AOG ratio on cell volume (12 h, 1200 °C). The red arrow indicates the cell volume of the sample prepared for NPD experiments. The color of the data points represents the sample color. Cell volumes are refined from XRPD data using an ~28.4 Å × 5.7 Å × 17.7 Å unit cell in space group *Imcb*, which is later shown to be the correct space group.

the Supporting Information), which could not be attributed to known impurity phases. It is shown below that these are due to a superstructure. The highest phase purity was obtained at 1200 °C, as shown in Figure 2a. The purest samples were yellow-ochre in color, whereas the least pure sample changed from red to black upon standing in air. This is consistent with oxidation of the impurity phase of red Ce_2O_2Se to black $Ce_2O_{2+x}Se$.[24]

Attempts were made to increase the phase purity by varying the final dwell time while maintaining the AOG molar amount at 110% and dwell temperature at 1200 °C (Figure 2b). Above 3 h, the dwell time makes little difference, producing samples of similar phase purity that are all yellow-ochre in color.

The effect of reducing the AOG molar ratio was also investigated at 1200 °C (Figure 2c). Phase purity is consistent (~97 wt %) between 110 and 100% AOG and then drops at 95 and 90%. One important aspect of this experiment is the generation of different minor impurity phases with varying AOG, as emphasized in the inset of Figure 2c. At 110 and 105% AOG, Ce_2O_2Se is the only impurity produced and has Ce in the 3+ oxidation state. Below 105% AOG, the Ce_2O_2Se amount decreases and is replaced by $Ce_4O_4Se_3$, CeO_2 (where Ce is in a 3+/4+ and 4+ oxidation state), and ZnSe. The increase in the oxidation state of Ce in these impurities is likely to be due to the increase in the amount of oxygen available when the AOG falls below the stoichiometric ratio.

During the synthesis, a small amount of an orange crystalline material (estimated at $\lesssim$0.005 g, 0.8% of the starting reagent mass) was typically observed on the quartz tube; XRPD revealed it to be ZnSe. This explains why the expected ZnSe impurity is often not present in the XRPD pattern when a small amount of Ce_2O_2Se impurity is present.

Effects of Synthetic Conditions on Structural and Physical Properties. In addition to influencing phase purity, the AOG quantity has a significant influence on the properties of the target phase. Figure 3 shows the colors of the samples, which correlate with the unit cell volume derived by powder

DOI: 10.1021/ic502551n
Inorg. Chem. 2015, 54, 1563−1571

diffraction. Figure 4a shows the effect of the final dwell temperature on cell volume. All samples have a similar cell volume, and the same yellow-ochre color (disregarding samples made at 1100 and 1150 °C, where the phase purity is low). Figure 4b shows the effect of the final dwell time on cell volume. As before, all samples have a similar cell volume and the same yellow-ochre color (disregarding the 1 h sample). Figure 4c shows the effect of the AOG quantity. This has a large effect on cell volume, and the change is accompanied by a gradual change in color, with samples being yellow-ochre, brown, and black at high, intermediate, and low cell volumes, respectively. At 90% AOG, the cell volume has increased relative to that of the 95% AOG sample, which is against the trend. Figure 2c suggests that at this low AOG ratio, the production of more oxidized impurity phases is favored over changes in the target phase. The sample made for PND measurements (see below) was black and had a cell volume of 2848.7(6) Å^3. This is comparable to the lowest cell volume sample prepared at 95% AOG, as indicated by the red arrow in Figure 4c.

The most likely cause of contraction in cell volume is the partial oxidation of Ce from 3+ to 4+. This effect has been seen in the related compound $CeOCu_{1-x}S$, which has been studied by several different groups.[11,25,26] Charge compensation in this system is achieved via loss of Cu^+, with reported samples ranging from near stoichiometric CeOCuS (dark olive green) to $CeOCu_{0.762}Se$ (jet black), with a reduction in cell volume of around 5%. If $Ce_2O_2ZnSe_2$ charge compensates via loss of Zn^{2+}, Zn loss is expected to be significantly lower. First, the reduction in cell volume is only around 0.4% in $Ce_2O_2ZnSe_2$ between the highest and lowest cell volumes synthesized. Second, the loss of only one Zn^{2+} ion is required to compensate for the oxidation of two Ce atoms. We can speculate that because the cell volume reduction in $Ce_2O_2ZnSe_2$ is less than 10% of that observed in $CeOCu_{0.762}Se$, and because Zn^{2+} loss can compensate for the oxidation two Ce atoms, the lowest cell volume sample would have a Zn content of >0.98.

Further support that this contraction is caused by partial oxidation of Ce comes from our ongoing work on solid solutions of various $Ln_2O_2MSe_2$-type phases. We find that changing the lanthanide leads to an approximately isotropic change in all lattice parameters, whereas substitution of M leads to a change mainly in the *c* direction, perpendicular to the layers. This is attributed to a relatively rigid Ln−O layer and a more flexible M−Se layer that adapts to the size demands of the Ln−O layer. Figure 5 shows the relative changes in cell parameters as a function of AOG quantity, when refined in the correct orthorhombic cell in space group *Imcb* with unit cell dimensions of ∼28.4 Å × ∼5.7 Å × ∼17.7 Å. The change of all cell parameters by roughly equal amounts as the AOG quantity is reduced suggests that contraction occurs in the Ln−O layer, as expected for partial oxidation of Ce, and that this dominates over Zn^{2+} loss in the more flexible M−Se layer.

Superstructure Investigation. Selected area electron diffraction (SAED) images were collected on the black, low cell volume NPD sample (Figure 6) and confirmed the presence of the superstructure reflections suggested from the PXRD patterns. Intense reflections consistent with the parent *P*4/*nmm* parent structure are labeled in white in Figure 6b; weak superstructure reflections are observed along [1$\bar{1}$0] and indexed in green. These are not present along [110], suggesting that the tetragonal symmetry has been lost. Figure 6c shows [110] zone axis data. It reveals no superstructure reflections

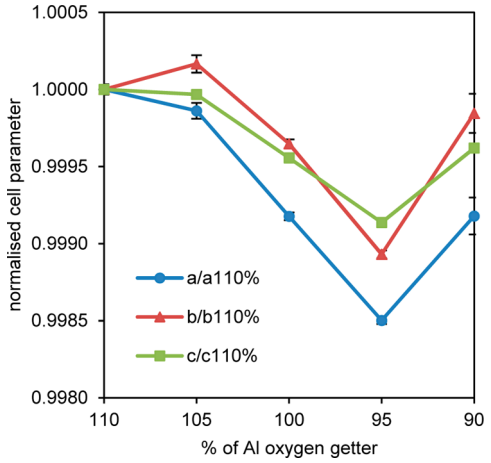

Figure 5. Effect of AOG molar quantity on normalized cell parameters.

along [001] or [110]; only reflections consistent with the parent structure are observed.

SAED images of $La_2O_2ZnSe_2$[15] revealed similar superstructure reflections, also exclusively along [1$\bar{1}$0], though at $^1/_4$ $^{\bar{1}}/_4$ 0, $^1/_2$ $^{\bar{1}}/_2$ 0, and $^3/_4$ $^{\bar{3}}/_4$ 0. These additional reflections were indexed as 200, 400, *h*00 (*h* = 2*n*) in a $4(2)^{1/2}a_{subcell} \times (2)^{1/2}a_{subcell} \times 2c_{subcell}$ unit cell. It therefore seemed likely that the $Ce_2O_2ZnSe_2$ structure may be related to the *P*4/*nmm* parent by a $5(2)^{1/2}a_{subcell} \times (2)^{1/2}a_{subcell} \times 2c_{subcell}$ unit cell. To confirm this supercell, Pawley refinements were attempted in the orthorhombic space group *P*222 with unit cell dimensions of ∼28.35 Å × ∼5.67 Å × ∼17.71 Å. This unit cell successfully accounts for all observed reflections in the powder data of the black, low cell volume NPD sample.

Development of the Crystal Structure Model. The crystal structure was solved with the help of web-based ISODISTORT software.[27] ISODISTORT calculates symmetry adapted distortion modes (displacive, site ordering, magnetic) associated with irreducible representations at different k-points. A low symmetry structure can then be described in terms of the parent structure and the amplitudes of the different ordering and displacive symmetry modes. This allows systematic and rapid exploration of different daughter structures from a given parent.

Compared to that of the parent, electron diffraction shows supercell diffraction peaks at ($^1/_5$ $^1/_5$ *g*) (Figure 6b), and Pawley refinement confirms that they can be explained with a $5(2a)^{1/2}{}_{subcell} \times (2a)^{1/2}{}_{subcell} \times 2c_{subcell}$ cell. The distortion vector of $Ce_2O_2ZnSe_2$ relative to the parent structure is therefore *S*(α α $^1/_2$), with α = $^1/_5$ or $^1/_{10}$ (due to systematic absences), and the representative basis is (supercell)

$$\begin{bmatrix} 5 & 5 & 0 \\ -1 & 1 & 0 \\ 0 & 0 & 2 \end{bmatrix} \begin{bmatrix} a_{subcell} \\ b_{subcell} \\ c_{subcell} \end{bmatrix} = \begin{bmatrix} a_{supercell} \\ b_{supercell} \\ c_{supercell} \end{bmatrix}$$

There are 16 possible daughter models within 6 space groups: *Cmma* (S_1 or S_3), *Cmca* (S_1, S_2, S_3, or S_4), and *Ccca* (S_2 or S_4) when α = $^1/_5$; and *Imma* (S_1 or S_3), *Ibam* (S_1, S_2, S_3, or S_4), and *Ibca* (S_2 or S_4) when α = $^1/_{10}$. Refinements were performed on the XRPD data of the black, low cell volume NPD samples for each of these 16 daughter models in which the amplitudes of S ordering and displacive modes were refined. The effect on the R_{wp} of the refinement is shown in Figure 7.

DOI: 10.1021/ic502551n
Inorg. Chem. 2015, 54, 1563−1571

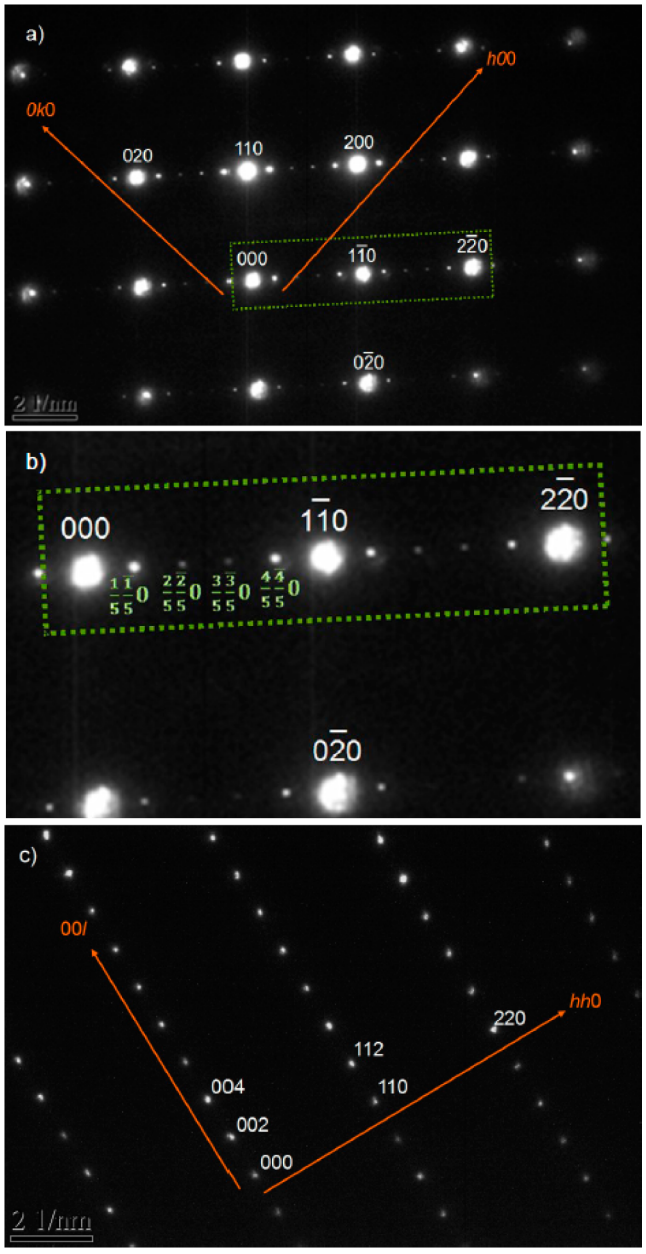

Figure 6. Selected area electron diffraction of $Ce_2O_2ZnSe_2$ taken down the (a) [001] zone axis, (b) enlarged [001] zone axis showing superstructure reflections, and (c) [1̄10] zone axis. Zone axes and *hkl* indices are given relative to the parent *P*4/*nmm* tetragonal cell. Reflections consistent with the parent structure are labeled in white; superstructure reflections are labeled in green.

There are two distorted models based on S_4 distortions, *Ibam* (72) and *Ibca* (73); both give significantly better agreement with the experimental data than others, both with R_{wp} = 2.53%. The ordering patterns of the Zn−Se layer in these two space groups are in Figure 8. In the *Ibam* (S_4) model, Zn^{2+} sites can be either fully occupied or fully vacant, whereas in the *Ibca* (S_4) model, there is one Wyckoff site 50% occupied by Zn^{2+} (shown as a half sphere in Figure 8b).

These two models are mathematically different though experimentally difficult to distinguish, even from "Rietveld quality" (14 h, 8−120° 2θ) laboratory powder diffraction data. Simulations show that the largest difference in the X-ray data between the two models should be the 110 reflection at 2θ ~16.4°, with an intensity of ~0.25% of the most intense peak; this peak is systematically absent in the *Ibca* model. A 54 h scan over a 2θ range of 15−21° was therefore collected; this reveals weak intensity for the 110 reflection (Figure 9). A good fit to these limited data was achieved using the Rietveld-derived model discussed below. We therefore selected the ordered *Ibam* (S_4) model for final Rietveld refinement.

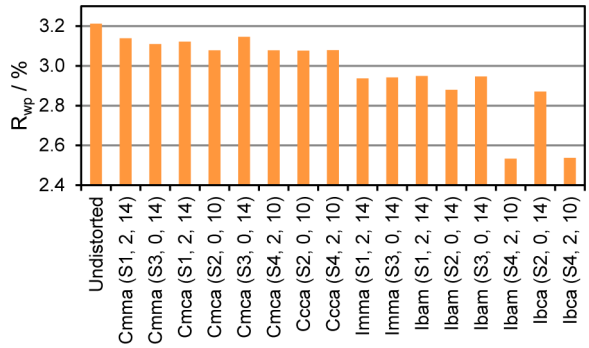

Figure 7. Refined R_{wp} for the $Ce_2O_2ZnSe_2$ XRPD pattern using different distorted models. The values in brackets give the specific S distortion mode label and the number of refined primary ordering and displacive modes.

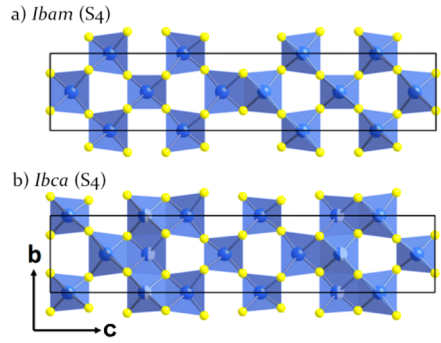

Figure 8. Zn ordering patterns in the Zn−Se layer of $Ce_2O_2ZnSe_2$ for (a) *Ibam* and (b) *Ibca* models from ISODISTORT refinement. Zn^{2+} cations are shown in blue, and Se^{2-} anions are shown in yellow. The 50% occupied site is shown as a half sphere.

Structure Refinement and Description. Final Rietveld refinements were performed on the fully cation-ordered model in space group *Imcb* (nonstandard setting of *Ibam* with the *c* axis perpendicular to the layers for consistency with other structures of this type reported in the literature) against X-ray and neutron powder data of the black, low cell volume PND sample; a total of 209 parameters were refined. Refinement of single O, Zn, and Se site occupancy gave a sample composition of $Ce_2O_2ZnSe_2$ within 3 standard uncertainties; hence, no indication of partial occupancy of Zn as charge compensation for partial Ce^{4+} formation could be detected. All sites were therefore considered fully occupied within the quality of the data. Refining separate temperature factors for each site did not significantly reduce R_{wp}; thus, a single temperature factor was refined for each atom type. Structural parameters are shown in Table 1. Selected Rietveld plots are shown in Figure 10 (all refinement profiles can be found in Figure S2 of the Supporting Information). Selected bond lengths and angles are given in Tables S1 and S2 of the Supporting Information, respectively. Figure 11 illustrates the structure of $Ce_2O_2ZnSe_2$.

$Ce_2O_2ZnSe_2$ contains alternating fluorite-like $[Ce_2O_2]^{2+}$ layers of Ce_4O tetrahedra and anti-fluorite-like $[ZnSe_2]^{2-}$

DOI: 10.1021/ic502551n
Inorg. Chem. 2015, 54, 1563−1571

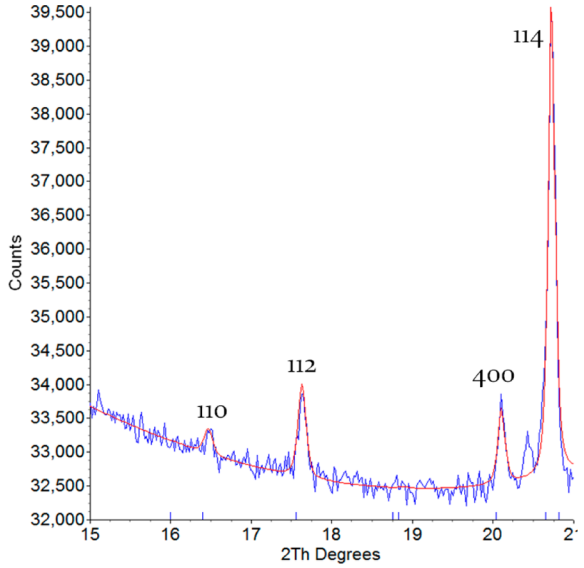

Figure 9. Rietveld refinement profile of $Ce_2O_2ZnSe_2$ XRPD data (54 h scan over the 2θ range of 15−21°) fitted using the ordered *Ibam* model. Data are consistent with an ∼0.25% intensity 110 reflection. The very weak peak at ∼20.5° is due to a ≲0.3% impurity.

layers perpendicular to the *c* axis of the material. It is closely related to the LnOCuCh-type structure except that the divalent nature of Zn^{2+} leads to half occupancy of the tetrahedral sites within the transition metal selenide layers.

The transition metal ordering pattern adopted in $Ce_2O_2ZnSe_2$ is novel yet closely related to those of other divalent transition metal containing compounds. It contains both edge-sharing and corner-sharing $ZnSe_4$ tetrahedra, leading to alternating "checkerboard-like" and "stripe-like" regions along the *a* axis. This is similar to the $La_2O_2ZnSe_2$ structure,[15] except $Ce_2O_2ZnSe_2$ has an extended checkerboard section. Using a simple nomenclature, we can describe the Ce material as 4C-1E and La as 3C-1E. Both $Ce_2O_2ZnSe_2$ and $La_2O_2ZnSe_2$ can therefore be considered intermediate structures between $Ce_2O_2FeSe_2$,[13] where all cations order in stripes of edge-sharing tetrahedra (0C-1E), and $La_2O_2CdSe_2$,[14] where all cations order in a checkerboard arrangement (1C-0E) of corner-sharing tetrahedra.

Although Zn ordering is the main driver for symmetry lowering, there are significant accompanying structural distortions, mainly in the Zn−Se tetrahedra shown in Figures 12 and 13. These are most pronounced in the edge-shared $Zn1Se_4$ tetrahedra and are reduced upon moving from $Zn2Se_4$ tetrahedra to $Zn3Se_4$ in the center of the corner-sharing block. As expected, the Zn−Zn separation in the edge-shared tetrahedra is significantly longer than an idealized structure [3.13(3) vs ∼2.84 Å]. Similar distortions are observed in the Zn−Se tetrahedra of $La_2O_2ZnSe_2$, where the edge-shared Zn−Zn separation is even greater (3.22 Å).[15] Distortions in the OCe_4 tetrahedra are less pronounced, though still considerable. This is most evident in the $O1Ce_4$ tetrahedron, which lies below the center of the corner-sharing block where $ZnSe_4$ tetrahedra are least distorted. A distortion mode analysis (see Table S3 and Figure S3 of the Supporting Information) shows that the four most significant structural distortions are S_4 modes on Zn ([100] direction), Se, Ce, and O (all in the [010] direction).

Cell Volume Dependence of the Zinc Ordering Pattern. The model presented above describes most of the $Ce_2O_2ZnSe_2$ samples synthesized; however, it describes those with lower cell volume better than those with higher cell volume. Figure 14a shows the XRPD patterns of the sample synthesized with a 3 h final dwell at 1200 °C and 110% AOG molar amount. This is the highest cell volume sample synthesized with sufficient phase purity (>95%) to clearly observe superstructure reflections. The structural model does not accurately describe the superstructure reflections.

Figure 14b−d shows the XRPD patterns of the samples synthesized with 105, 100, and 95% AOG, respectively (all at 1200 °C for 12 h), which represent samples with systematically decreasing cell volume (Figure 4c). The structural model provides a progressively better fit to superstructure reflections as the cell volume decreases. Figure 14e shows the XRPD pattern of the sample synthesized for NPD experiments, which has the lowest cell volume and gives an excellent fit to the structural model presented.

Ongoing work suggests that superlattice peaks in the samples represented in Figure 14a−d are incommensurately modulated due to a size mismatch between $[Ce_x^{4+}Ce_{2-x}^{3+}O_2]^{(2+x)+}$ and zinc selenide layers. For the low cell volume sample in Figure 14e, this locks in to the commensurate structure presented.

Diffuse Reflectance Spectroscopy. Diffuse reflectance spectroscopy (DRS) reveals different band gaps for high, intermediate, and low cell volume $Ce_2O_2ZnSe_2$ samples, which is unsurprising on the basis of their different colors. The high cell volume yellow-ochre sample, intermediate cell volume

Table 1. Structural Parameters of $Ce_2O_2ZnSe_2$ from Combined Refinement Using Room-Temperature XRPD and NPD Data[a]

site label	Wyckoff site	*x*	*y*	*z*	*B* (Å²)	valence
Ce(1)	16k	0.1992(3)	0.741(1)	0.3191(4)	0.47(2)	3.19
Ce(2)	16k	0.3998(3)	0.770(1)	0.3188(4)	0.47(2)	3.26
Ce(3)	8j	0	0.777(1)	0.8200(6)	0.47(2)	3.16
O(1)	8g	0.75	0	0.2560(4)	0.63(3)	2.24
O(2)	16k	0.8504(3)	0.486(3)	0.2499(2)	0.63(3)	2.41
O(3)	16k	−0.0501(4)	−0.025(2)	0.2517(3)	0.63(3)	2.31
Zn(1)	8i	0.0551(3)	0.5	0	1.19(3)	1.76
Zn(2)	8h	0.1515(4)	0	0	1.19(3)	1.96
Zn(3)	4b	0.75	0	0.5	1.19(3)	2.03
Se(1)	16k	0.7002(4)	0.254(1)	0.0831(3)	0.87(2)	1.82
Se(2)	16k	0.8991(3)	0.2305(8)	0.0878(2)	0.87(2)	1.85
Se(3)	8j	0	0.725(1)	0.0845(5)	0.87(2)	1.77

[a]Space group *Imcb*, a = 28.3595(4) Å, b = 5.67087(8) Å, c = 17.71308(6) Å, R_{wp} = 1.848%, R_p = 1.081%, and χ^2 = 1.193. Occupancy for all sites is 1.

DOI: 10.1021/ic502551n
Inorg. Chem. 2015, 54, 1563−1571

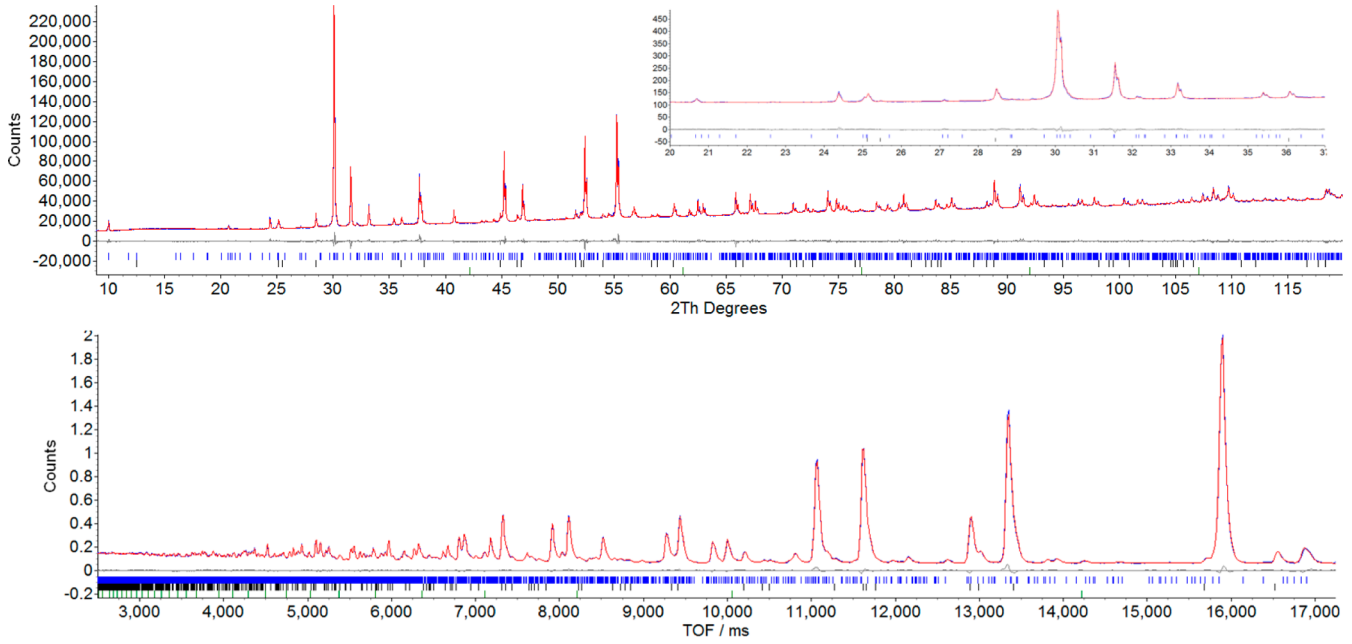

Figure 10. Rietveld refinement profiles from combined refinement using room-temperature (top) XRPD and (bottom) NPD data for $Ce_2O_2ZnSe_2$. Tick marks show reflection positions for $Ce_2O_2ZnSe_2$ (blue, ~95% by weight), Ce_2O_2Se (black, ~5% by weight), and vanadium (green, from sample used in PND data collection).

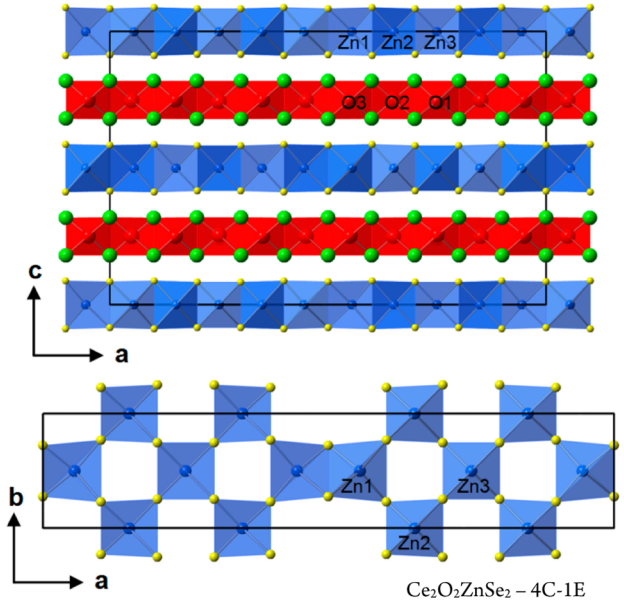

Figure 11. (top) $Ce_2O_2ZnSe_2$ structure with sheets of edge-sharing Ce_4O (red) and $ZnSe_4$ tetrahedra (blue), viewed down [010]. (bottom) View down [001] showing a mix of stripe-like edge-sharing $ZnSe_4$ tetrahedra and checkerboard-like corner-sharing $ZnSe_4$ tetrahedra (4C-1E), with an extended checkerboard-like section relative to $La_2O_2ZnSe_2$.

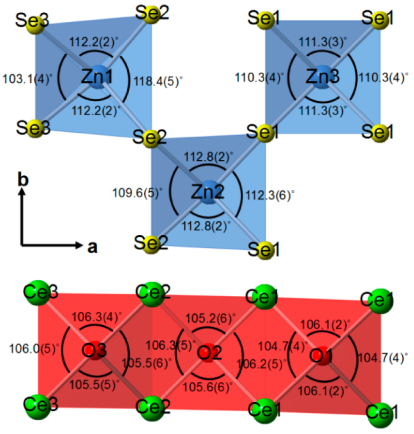

Figure 12. Coordination environments of Zn and O sites viewed down [001].

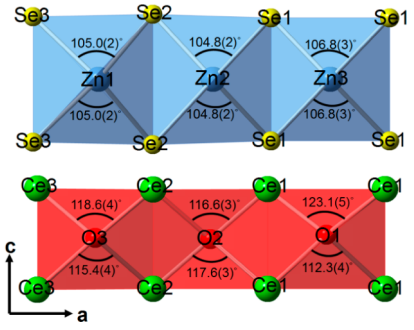

Figure 13. Coordination environments of Zn and O sites viewed down [010].

brown sample, and low cell volume black sample have band gaps of ~2.2, ~1.4, and ~1.3 eV, respectively, as shown in Figure 15. Narrowing of the band gap is not linearly dependent on cell volume. Measured band gaps are significantly smaller than for $La_2O_2ZnSe_2$ (3.4 eV)[15] and are strongly influenced by Ce(IV) content.

Magnetic Properties. The temperature dependence of the molar magnetic susceptibility (χ_{mol}) of $Ce_2O_2ZnSe_2$ (NPD sample) is shown in Figure 16. $Ce_2O_2ZnSe_2$ is a typical paramagnet and obeys the Curie–Weiss law from 150 to 300 K. By Curie–Weiss fitting $1/\chi_{mol} - T$ data from 150 to 300 K, we obtain an effective magnetic moment of Ce_2O_2ZnSe of μ_{eff} = 3.43(1) μ_B, which equates to μ_{eff} = 2.42(1) μ_B for each

DOI: 10.1021/ic502551n
Inorg. Chem. 2015, 54, 1563–1571

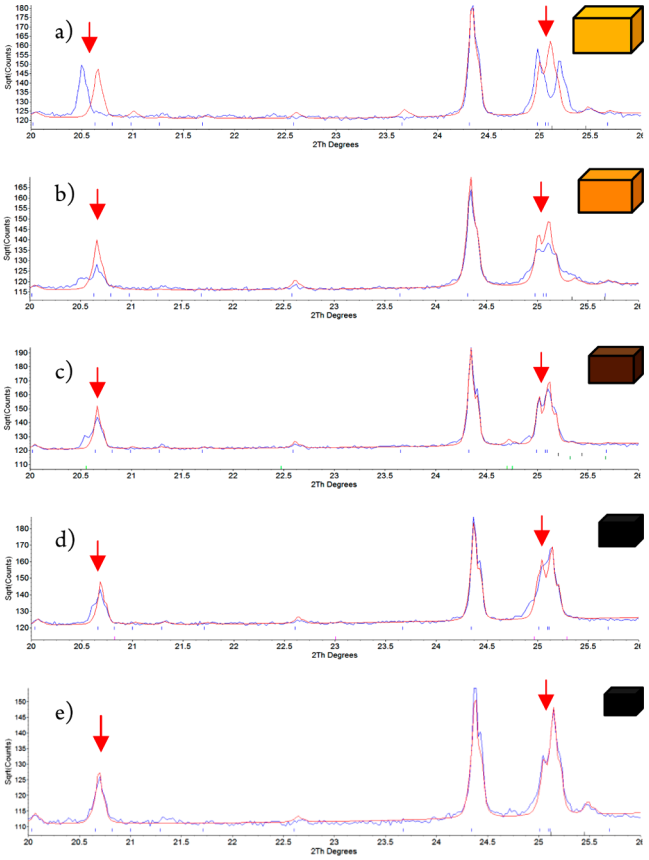

Figure 14. Rietveld fits of XRPD patterns of $Ce_2O_2ZnSe_2$ samples with systematically decreasing cell volume from (a) to (e) as shown by the cuboids. The cuboid's color represents the sample color. The structural model proposed provides a good fit to superstructure reflections (marked by red arrows) for the minimum cell volume samples.

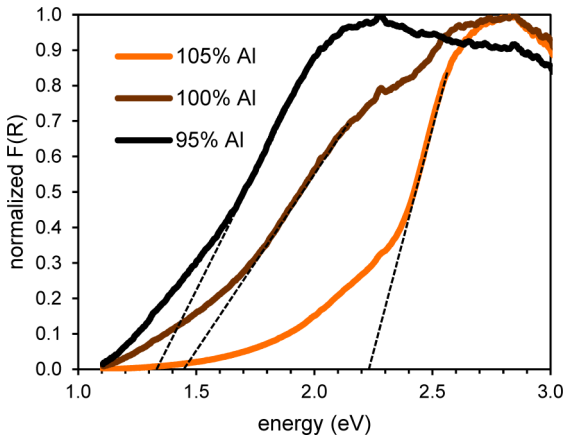

Figure 15. Normalized diffuse reflectance spectra after Kubelka–Munk treatment for $Ce_2O_2ZnSe_2$ samples synthesized with 105% AOG (yellow), 100% AOG (brown), and 95% AOG (black) showing interband transitions corresponding to an optical band gap of ~2.2, ~1.4, and ~1.3 eV, respectively.

$CeOZn_{0.5}Se$. In $Ce_2O_2ZnSe_2$, the magnetic properties come from the $4f^1$ open shell ion Ce^{3+}. The ground state of Ce^{3+} is $^2F_{5/2}$ with a theoretical effective magnetic moment μ_{eff} = 2.54 μ_B; however, most experimental results of Ce^{3+} show that $\mu_{eff} \cong$ 2.4 μ_B.[28] The Weiss constant θ is −10(2) K, indicating local

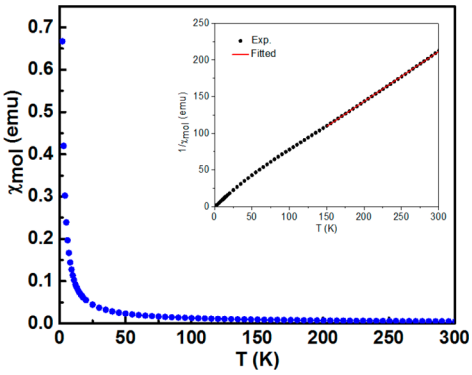

Figure 16. Molar susceptibility of $Ce_2O_2ZnSe_2$ at different temperatures.

antiferromagnetic interactions; however, we do not observe the onset of long-range order down to 2 K. Similar behavior has been reported for $Ln_4O_4Se_3$ (Ln = Ce and Nd) systems.[29]

CONCLUSION

We describe here the synthesis, structural characterization, optical measurements, and magnetic measurements of the new material $Ce_2O_2ZnSe_2$. It adopts a ZrCuSiAs-related structure with ordering of Zn^{2+} cations over the tetrahedral sites in the $[ZnSe_2]^{2-}$ layers. The ordering pattern contains both corner-sharing and edge-sharing tetrahedra and is intermediate between ordering patterns observed for $Ce_2O_2FeSe_2$ and $La_2O_2CdSe_2$. It is similar to $La_2O_2ZnSe_2$ except that $Ce_2O_2ZnSe_2$ has extended corner-sharing regions.

The color of the compound changes as a function of cell volume, which varies by ~0.4%. At the highest, intermediate, and lowest cell volume, the compound color is yellow-ochre, brown, and black, respectively. This decrease is attributed to partial oxidation of the Ce from 3+ to 4+, the extent of which can be controlled by synthetic conditions.

$Ce_2O_2ZnSe_2$ is a semiconductor in all cases with experimental optical band gaps of 2.2, 1.4, and 1.3 eV for the samples colored yellow-ochre, brown, and black, respectively. SQUID measurements show $Ce_2O_2ZnSe_2$ to be paramagnetic down to 2 K.

ASSOCIATED CONTENT

Supporting Information

Rietveld refinement profiles for refinement of the ZrCuSiAs structural model for $Ce_2O_2ZnSe_2$; Rietveld refinement profiles for the *Imcb* model; bond lengths; bond angles; table of occupancy mode number, atom type, mode label, k-point, and order parameter direction; histogram showing the most significant structural distortions; and a cif file of the final refinement. This material is available free of charge via the Internet at http://pubs.acs.org.

AUTHOR INFORMATION

Corresponding Author

*E-mail: john.evans@durham.ac.uk.

Notes

The authors declare no competing financial interest.

ACKNOWLEDGMENTS

We thank ISIS for neutron time. We are grateful to Dr. Budhika Mendis for assistance during electron diffraction measurements,

DOI: 10.1021/ic502551n
Inorg. Chem. 2015, 54, 1563−1571

Andrew Duckworth for assistance with DRS measurements, and Dr. Johan Buurma for SQUID measurements. We thank EPSRC for funding.

REFERENCES

(1) Kamihara, Y.; Watanabe, T.; Hirano, M.; Hosono, H. *J. Am. Chem. Soc.* **2008**, *130*, 3296−3297.
(2) Mizuguchi, Y.; Fujihisa, H.; Gotoh, Y.; Suzuki, K.; Usui, H.; Kuroki, K.; Demura, S.; Takano, Y.; Izawa, H.; Miura, O. *Phys. Rev. B* **2012**, *86*, 5.
(3) Singh, S. K.; Kumar, A.; Gahtori, B.; Shruti; Sharma, G.; Patnaik, S.; Awana, V. P. S. *J. Am. Chem. Soc.* **2012**, *134*, 16504−16507.
(4) Tan, S. G.; Li, L. J.; Liu, Y.; Tong, P.; Zhao, B. C.; Lu, W. J.; Sun, Y. P. *Phys. C (Amsterdam, Neth.)* **2012**, *483*, 94−96.
(5) Yazici, D.; Huang, K.; White, B. D.; Chang, A. H.; Friedman, A. J.; Maple, M. B. *Philos. Mag.* **2012**, *93*, 673−680.
(6) Krzton-Maziopa, A.; Guguchia, Z.; Pomjakushina, E.; Pomjakushin, V.; Khasanov, R.; Luetkens, H.; Biswas, P. K.; Amato, A.; Keller, H.; Conder, K. *J. Phys.: Condens. Matter* **2014**, *26*, 5.
(7) Phelan, W. A.; Wallace, D. C.; Arpino, K. E.; Neilson, J. R.; Livi, K. J.; Seabourne, C. R.; Scott, A. J.; McQueen, T. M. *J. Am. Chem. Soc.* **2013**, *135*, 5372−5374.
(8) Sathish, C. I.; Feng, H. L.; Shi, Y. G.; Yamaura, K. *J. Phys. Soc. Jpn.* **2013**, *82*, 6.
(9) Ueda, K.; Inoue, S.; Hirose, S.; Kawazoe, H.; Hosono, H. *Appl. Phys. Lett.* **2000**, *77*, 2701−2703.
(10) Hiramatsu, H.; Yanagi, H.; Kamiya, T.; Ueda, K.; Hirano, M.; Hosono, H. *Chem. Mater.* **2008**, *20*, 326−334.
(11) Ueda, K.; Takafuji, K.; Hiramatsu, H.; Ohta, H.; Kamiya, T.; Hirano, M.; Hosono, H. *Chem. Mater.* **2003**, *15*, 3692−3695.
(12) Ijjaali, I.; Mitchell, K.; Haynes, C. L.; McFarland, A. D.; Van Duyne, R. P.; Ibers, J. A. *J. Solid State Chem.* **2003**, *176*, 170−174.
(13) McCabe, E. E.; Free, D. G.; Evans, J. S. O. *Chem. Commun. (Cambridge, U.K.)* **2011**, *47*, 1261−1263.
(14) Hiramatsu, H.; Ueda, K.; Kamiya, T.; Ohta, H.; Hirano, M.; Hosono, H. *J. Mater. Chem.* **2004**, *14*, 2946−2950.
(15) Tuxworth, A. J.; McCabe, E. E.; Free, D. G.; Clark, S. J.; Evans, J. S. O. *Inorg. Chem.* **2013**, *52*, 2078−2085.
(16) Rietveld, H. M. *J. Appl. Crystallogr.* **1969**, *2*, 65.
(17) Coelho, A. A. *J. Appl. Crystallogr.* **2003**, *36*, 86−95.
(18) Coelho, A. A. *TOPAS Academic: General Profile and Structure Analysis Software for Powder Diffraction Data*, 5th ed.; Bruker AXS: Karlsruhe, Germany, 2012.
(19) Coelho, A. A.; Evans, J. S. O.; Evans, I. R.; Kern, A.; Parsons, S. *Powder Diffr.* **2011**, *26*, S22−S25.
(20) Dollase, W. *J. Appl. Crystallogr.* **1986**, *19*, 267−272.
(21) Pitschke, W.; Hermann, H.; Mattern, N. *Powder Diffr.* **1993**, *8*, 74−83.
(22) Kortum, G.; Braun, W.; Herzog, G. *Agnew. Chem., Int. Ed.* **1963**, *2* (7), 333−404.
(23) Tandon, S. P.; Gupta, J. P. *Phys. Status Solidi* **1970**, *38*, 363−367.
(24) Benacerraf, A.; Guittard, M.; Domange, L.; Flahaut, J. *Bull. Soc. Chim. Fr.* **1959**, 1920−1922.
(25) Chan, G. H.; Deng, B.; Bertoni, M.; Ireland, J. R.; Hersam, M. C.; Mason, T. O.; Van Duyne, R. P.; Ibers, J. A. *Inorg. Chem.* **2006**, *45*, 8264−8272.
(26) Pitcher, M. J.; Smura, C. F.; Clarke, S. J. *Inorg. Chem.* **2009**, *48*, 9054−9056.
(27) Campbell, B. J.; Stokes, H. T.; Tanner, D. E.; Hatch, D. M. *J. Appl. Crystallogr.* **2006**, *39*, 607−614.
(28) Frederikse, H. P. R. In *CRC Handbook of Chemistry and Physics*, 84th ed.; Lide, D. R., Ed.; CRC Press: Boca Raton, FL, 2004; pp 12−117.
(29) Strobel, S.; Choudhury, A.; Dorhout, P. K.; Lipp, C.; Schleid, T. *Inorg. Chem.* **2008**, *47*, 4936−4944.

DOI: 10.1021/ic502551n
Inorg. Chem. 2015, 54, 1563−1571